ENVIRONMENTAL RESEARCH
CLIMATE

PAPER • OPEN ACCESS

Observable polar and Atlantic sea surface salinity trends have emerged, while the noisy Indo-Pacific hesitates

To cite this article: David P Schneider *et al* 2025 *Environ. Res.: Climate* **4** 045002

View the article online for updates and enhancements.

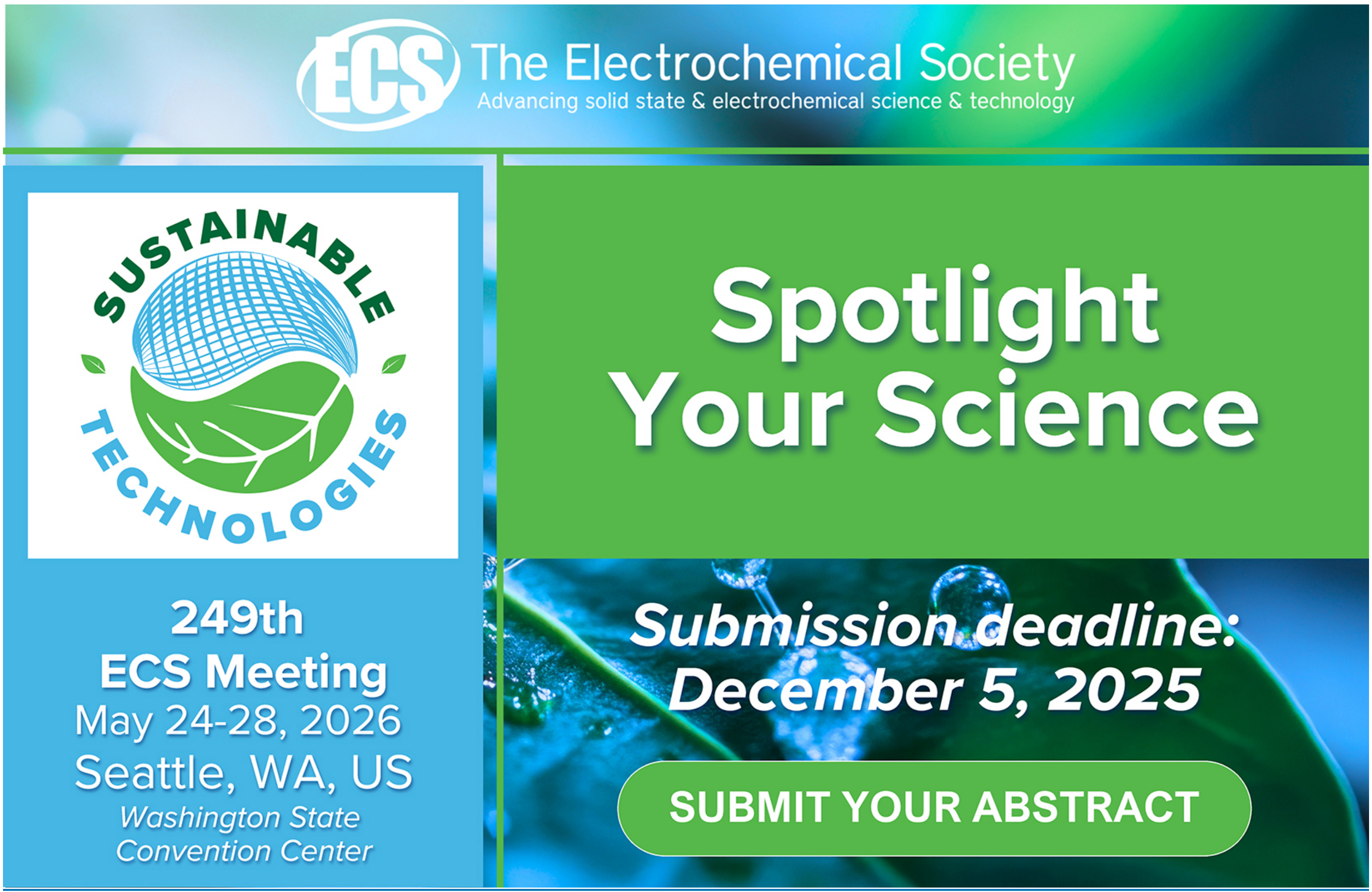

IOP Publishing Environ. Res.: Climate 4 (2025) 045002 https://doi.org/10.1088/2752-5295/ae065b

ENVIRONMENTAL RESEARCH
CLIMATE

OPEN ACCESS

RECEIVED
23 May 2025

REVISED
27 August 2025

ACCEPTED FOR PUBLICATION
12 September 2025

PUBLISHED
23 September 2025

PAPER

Observable polar and Atlantic sea surface salinity trends have emerged, while the noisy Indo-Pacific hesitates

David P Schneider[1,*], **Nicola Maher**[2,3], **Yue Dong**[4], **Jennifer E Kay**[1,5] and **Antonietta Capotondi**[1,6]

[1] Cooperative Institute for Research in Environmental Sciences, University of Colorado Boulder, Boulder, CO, United States of America
[2] Australian National University, Canberra, Australia
[3] Australian Research Council Centre of Excellence for Weather of the 21st Century, Canberra, Australia
[4] Department of Atmospheric and Oceanic Sciences, University of California Los Angeles, Los Angeles, CA, United States of America
[5] Department of Atmospheric and Oceanic Sciences, University of Colorado Boulder, Boulder, CO, United States of America
[6] Physical Sciences Laboratory, National Oceanic and Atmospheric Administration, Boulder, CO, United States of America
[*] Author to whom any correspondence should be addressed.

E-mail: David.Schneider-1@colorado.edu

Keywords: sea surface salinity, time of emergence, climate change, large ensembles, CMIP6 models

Supplementary material for this article is available online

Abstract

The sea surface salinity (SSS) trend pattern is widely accepted as a fingerprint of hydrologic cycle intensification, and more tentatively as an indicator of Atlantic Meridional Overturning Circulation (AMOC) weakening. As these systematic changes imply consequential impacts, it is important to know when the signal of forced SSS change emerges above the noise of internal climate variability, and what drives this signal. We estimate time of emergence of global SSS change across four, single-model initial-condition large ensembles (LEs) spanning the 20th and 21st Centuries. We also compare the climatology, variability, and trend patterns in these models to estimates from two observational datasets. Consistently across the LEs, the SSS signal first emerges (as early as 1990s) in the central Arctic and subtropical north Atlantic, and parts of the Southern Ocean. Across most of the Indo-Pacific, the signal does not emerge until after 2050. The global SSS trend pattern broadly follows the 'fresh get fresher, salty get saltier' signature of hydrologic cycle intensification, but additional processes—including AMOC weakening, sea ice loss and vertical mixing—boost the signals in the Atlantic basin and polar regions. When attributing the observed trends, independent models demonstrate that greenhouse gases (GHGs) are essential for explaining the global-scale pattern of freshening in the Pacific while the Atlantic gets saltier. According to one of the best-performing models, anthropogenic aerosols have muted the GHG-driven signal, delaying the emergence of the Atlantic salting trend and north Pacific freshening trend by up to three decades. In the Indo-Pacific, SSS trends are affected by large internal variability, the interplay of aerosol-driven and GHG-driven signals, and attenuation by vertical mixing and surface currents. Looking forward, all models project that the established global SSS trend pattern will intensify. Continued SSS observations in conjunction with model evaluation will help distinguish among possible futures in the tropical Indo-Pacific.

1. Introduction

The global ocean has been described as the largest rain gauge on Earth (e.g. Schmitt 2008, Terray *et al* 2012, Douville and Cheng 2024). Long-term changes in ocean surface properties, particularly sea surface salinity (SSS), reflect changes in evaporation (E) and precipitation (P), and more broadly, the intensification of the hydrologic cycle. Recent advances in observing SSS from spaceborne platforms (e.g. Melnichenko *et al* 2016, 2021) and long-term reconstructions based on compilations of *in situ* data (e.g. Cheng *et al* 2020) provide promising opportunities to understand changes in the hydrologic cycle and to evaluate model performance. Projected changes in the hydrologic cycle under greenhouse-gas (GHG)-driven warming are highly model dependent (e.g. Lehner *et al* 2020), limiting society's ability to plan for and adapt to change. The promise of SSS as a gauge of consequential change is further underscored by its potential to track expected changes in ocean stratification (Capotondi *et al* 2012) and ocean dynamics, especially the weakening of the Atlantic Meridional Overturning Circulation (AMOC) (e.g. Zhu and Liu 2020, Zhu *et al* 2023, Li and Liu 2025). A recent study summarizes these and other processes and their effects on the salinity distribution (Lu *et al* 2024).

Although recognized as a fingerprint of hydrologic cycle intensification and of changes in ocean dynamics, whether the oceanic SSS gauge can be reliably calibrated to provide useful constraints on projections remains a matter of debate. Durack *et al* (2012) used observed and modeled SSS to infer a global-mean hydrologic cycle intensification rate of 8% / °C, but subsequent studies have inferred lower rates of around 3% – 5% / °C (e.g. Skliris *et al* 2016, Cheng *et al* 2020). Recently, Douville and Cheng (2024) introduced the Global Sea Surface Salinity Contrast (GSSSC) index, which is a measure of the 'fresh get fresher, salty get saltier' paradigm. Although they found support for this paradigm in both observations and models, their results depended on both the selected domain and the model being used. They did find some consistency across the models and observations, leading them to emphasize that the 'fresh get fresher' part is more robust than the 'salty get saltier' part.

The goal of this study is not to attempt another calibration of the salinity gauge, but instead a further refinement of the 'fresh get fresher, salty get saltier' paradigm. Our framework is the time of emergence (ToE) of the salinity signal, utilizing large ensembles (LEs) to robustly separate signal from noise, and to make an accurate assessment of model biases, some of which may influence the ToE. We also emphasize that other large-scale processes beyond hydrologic cycle intensification need to be considered to fully explain SSS trends. We use multiple models to illustrate consistent patterns of SSS change among the models and between models and observations. Applying the ToE metric (e.g. Hawkins and Sutton 2012), which formally separates signal from noise, we focus on the two-part question, '*When does the signal of SSS change emerge above the noise of internal climate variability, and what drives the signal?*' Answering this question can help society prepare for significant climate impacts, as it is a way of projecting when certain aspects of the climate system are operating outside the familiar bounds of internal variability. This can also help inform the design of observing systems, for example, by guiding where long-term instruments should be deployed in order to detect significant change and provide an observational record for evaluating models.

Previous work has at least indirectly answered the above question but has found mixed results, instilling a lack of confidence in model projections and some confusion about the interpretation of the observed SSS trends. Using CMIP3-era models and an early SSS reconstruction, Durack *et al* (2012) argue (without undertaking a formal ToE analysis) that the anthropogenic, warming-driven SSS signal had already emerged by the year 2000 across the global ocean. They conclude that the CMIP3 models underestimated the rates of salinity and hydrologic change. Since then, the increased availability of single-model initial-condition LEs has enabled a more thorough understanding of uncertainty in model projections, and a fairer comparison of observations and models. Specifically, LEs permit the quantification and partitioning of uncertainty arising from three primary sources: Model physics (or structural); emissions scenario; and internal variability (e.g. Lehner *et al* 2020, Maher *et al* 2020). With this in mind, Schlunegger *et al* (2020) present a survey of ocean biogeochemical change across multiple LEs, including ToE for salinity. They find that SSS has a long, 50+ year timescale of emergence. In striking contrast to Durack *et al* (2012), they write that for SSS, 'the observational record is likely insufficient for even global anthropogenic trends to be identified.'

Schlunegger *et al* (2020) do not present an observational analysis nor an observational-model comparison. One such comparison is presented in Cheng *et al* (2020), who find that the observed, accelerating salinity contrast (SC) between salty and fresh areas of the global ocean can only be explained by model simulations that apply anthropogenic forcing. From their methodology, which compares experiments forced only with natural forcings to those including both natural and anthropogenic forcing, they conclude that the global-mean SSS contrast has a 25-year timescale of emergence under the anthropogenic forcing of the late 20th Century. Cheng *et al* (2020) do not consider the emergence of the SSS signal on a regional or local grid box basis.

The novelty of the present study is to combine an apples-to-apples observational-model comparison with a pointwise ToE analysis applied to multiple LEs, including selected single-forcing LEs. We are also motivated by the quantification of the 'fresh get fresher, salty get saltier' trend pattern presented by Douville and Cheng (2024). We illustrate how this pattern evolves in multiple LEs and add our own metric for the amplification of the climatological salinity patterns. We expand previous storylines of SSS change to include the role of internal variability and highlight the apparent signatures of processes besides precipitation and evaporation, namely sea ice melt and AMOC weakening.

2. Data and methods

2.1. LE data

As listed in table 1, we use output from five different CMIP5- and CMIP6- era models. Our core analyses are based on the four LEs that combine the historical and near-future time periods with all anthropogenic and natural forcings evolving: CESM1-LE (Kay *et al* 2015), CESM2-LE (Rodgers *et al* 2021), the MPI CMIP6 Grand Ensemble (Olonscheck *et al* 2023), and the GISS-E2-1-G CMIP6 ensemble (Kelley *et al* 2020). This selection offers a diversity of models (with different model physics, different climate sensitivities, etc) while enabling a succinct analysis within the scope of available data and resources. These are widely used and well evaluated ESMs that have contributed to the CMIP5 and CMIP6 projects; details on the experiments and models themselves are given in the references in table 1.

To understand more clearly the signals from GHGs alone, we extend our analyses using the CESM2-GHG single-forcing LE (Simpson *et al* 2023). Two more ensembles from different models are used to verify the GHG driven signal: CESM1-xGHG (where all but evolving GHG concentrations are prescribed; Deser *et al* 2020a), and MIROC6-GHG (Shiogama *et al* 2023). Previous work uses single-forcing ensembles to distill the evolving SSS trend patterns due to aerosols and GHGs over the historical period (Dong *et al* 2024); here we examine how well the GHG-driven trend explains the observed trend and highlight the role of GHGs in driving the ToE of SSS change. Finally, we use the CESM1-xAER ensemble (Deser *et al* 2020a) to highlight the role of anthropogenic aerosols in delaying the emergence of the GHG-driven signal.

From each ensemble, we analyze four primary surface variables from the monthly output: SSS, sea surface temperature (SST), evaporation (E), and precipitation (P). The SST and SSS fields are regridded from their native resolution to a common 1° grid using bilinear interpolation. Annual means for SSS and SST are formed by taking 12 month averages, while for E and P the individual monthly totals are summed for each year. The calculations described below are performed on the annual means.

2.2. Observational data

We employ two observational data products of SSS. The first is the Multi-Mission Optimally Interpolated SSS Monthly Dataset, version 2 (OISSSv2; IPRC/SOEST University of Hawaii 2023), which is produced at 0.25° horizontal resolution. Building on the original SSS product based on L-band radiometer measurements from the Aquarius satellite (Melnichenko *et al* 2016), the dataset now combines observations from three satellite missions, offering regular updates and the ability to monitor ongoing ocean surface change at relatively high spatial and temporal resolutions (Melnichenko *et al* 2021). However, OISSSv2, commencing in 2011, provides too short of a record to confidently evaluate long-term change in the context of internal variability. Therefore, we also use a salinity reconstruction from the Institute of Atmospheric Physics (IAP) of the Chinese Academy of Sciences, described in Cheng *et al* (2020). Hereafter referred to as the 'IAP' dataset, this dataset incorporates many *in situ* measurements and interpolates them to a spatially complete field. The dataset spans 1940 to the near present at 1° spatial resolution and a monthly timestep. It is vertically resolved, covering the upper ∼2000 m of the ocean. Here, we only use the uppermost layer (0–1 m). To appreciate observational uncertainty as well as the differences between the IAP dataset and other long-term salinity reconstructions, we refer the reader to Cheng *et al* (2020) and Bao *et al* (2019).

Although OISSSv2 and IAP are derived from independent source data, it should be noted that the OISSSv2 processing algorithm involves bias corrections to ARGO float data, which are one of the main inputs to the IAP analysis. In addition, the IAP dataset uses spatial covariance information from models to inform its interpolation algorithm. In practice, the annual climatologies, interannual variability patterns, and short-term trends of the two datasets are quite similar (figure S1). Based on communication with an author of the IAP dataset, and our own interpretation of the results, we are confident using the IAP data to evaluate large-scale trend patterns since 1950. This time horizon makes the long-term pattern of change readily visible, avoiding short-term trends that might be strongly influenced by interannual or decadal modes of internal variability. As needed to facilitate direct comparisons, we regrid the IAP and OISSSv2 data to the same 1° grid as the model output.

2.3. ToE

The ToE is a signal-to-noise metric that defines when the signal of interest statistically emerges above the noise of the system. The application of ToE to the detection of ocean surface change in LEs is described in detail in Schlunegger *et al* (2020). Here, the 'signal' is the forced response to anthropogenic perturbations of the atmospheric composition, estimated as the ensemble-mean trend of a LE. The 'noise' is estimated by calculating the standard deviation of the corresponding trends across the individual ensemble members. The ToE is the first year when the magnitude of the signal is twice the magnitude of the noise, i.e. the

Table 1. List and key details of the eight model—experiment pairs evaluated in this study. **Bolded models** are CMIP6-generation models consistently using CMIP6 historical forcing and SSP370 scenario forcing, facilitating the most apples-to-apples comparisons of mean state and ToE for ocean surface properties.

Model/experiment *key scientific reference*	Time period	Forcing	Ensemble size	Data source/data reference
CESM1-LE Kay *et al* (2015)	1920–2100	Hist through 2005; RCP8.5	40	Kay *et al* (2025). CESM1 Large Ensemble Community Project [Dataset]. NSF National Center for Atmospheric Research https://doi.org/10.5065/D6J101D1
CESM1-xGHG Deser *et al* (2020)	1920–2080	Hist through 2005; RCP8.5	20	Same as above
CESM1-xAER Deser *et al* (2020)	1920–2080	Hist through 2005; RCP8.5	20	Same as above
CESM2-LE CMIP6 Rodgers *et al* (2021)	1850–2100	Hist through 2014; SSP370	50	Danabasoglu *et al* (2021). CESM2 Large Ensemble Community Project [Dataset]. NSF National Center for Atmospheric Research. https://doi.org/10.26024/KGMP-C556
CESM2-GHG Simpson *et al* (2023)	1850–2050	Hist through 2014; SSP370	15	Simpson and Rosenbloom (2022). CESM2 Single Forcing Large Ensemble Project [Dataset]. NSF National Center for Atmospheric Research. https://doi.org/10.26024/YW4W-1W27
MPI-ESM 1.2 LR (CMIP6 Grand Ensemble) Olonscheck *et al* (2023)	1850–2100	Hist through 2014; SSP370	30	DKRZ https://esgf-data.dkrz.de/search/cmip6-dkrz/
GISS-E2-1-G Kelley *et al* (2020)	1850–2100	Hist through 2014; SSP370	10 (all members use the same physics)	CMIP6 archive https://aims2.llnl.gov/search/cmip6/
MIROC6-GHG Shiogama *et al* (2023)	1850–2100	Hist through 2020; SSP245	50	CMIP6 archive https://aims2.llnl.gov/search/cmip6/

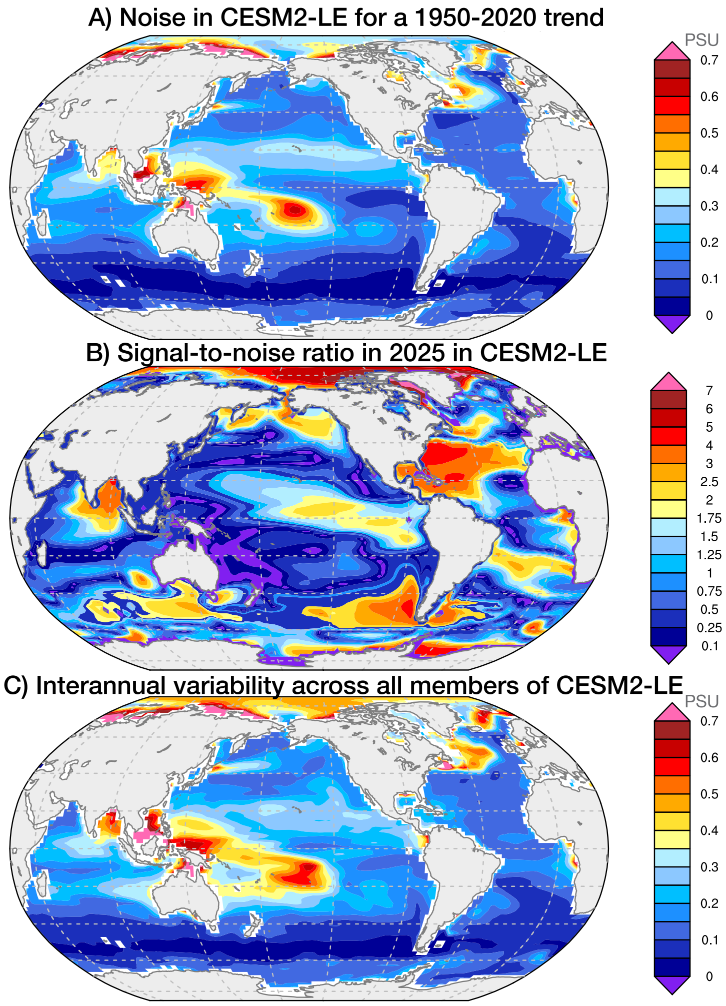

Figure 1. (a) Snapshot of the noise in CESM2-LE for a 1950–2020 trend in SSS. As defined in methods for ToE analysis, noise is calculated as the standard deviation of trends across the ensemble members. For illustration purposes to exaggerate the noise structure, the gridpoint values are scaled by 170; (b) signal-to-noise ratio (SNR) in 2025 for a 1950–2025 trend in SSS according to CESM2-LE. This is the definition used in ToE analysis as discussed in methods; values of 2 or greater (warm colors) indicate emergence of the SSS signal by 2025 or earlier. (c) Interannual variability of SSS across all 50 members of CESM2-LE. The interannual standard deviation for 1951–2000 was found for each gridpoint for each ensemble member separately, then averaged across the 50 members. For illustration, values are scaled by twice the square root of 50.

signal-to-noise ratio (SNR) is greater than or equal to two. This threshold implies that the signal is statistically significant at the 95% confidence level.

The concept of noise is closely related to internal variability, which arises from natural processes that govern the interactions among the ocean, atmosphere, land, biosphere, and cryosphere components of the coupled Earth system (e.g. Deser *et al* 2020). In our framework, internal variability is the deviation of a given ensemble member from the ensemble mean; it is represented by the ensemble spread, which arises from the slightly different initial conditions of each ensemble member.

We perform our ToE calculations on the annual mean fields for trends starting in 1950. Starting with a 1950–1970 trend, trends are calculated on a 5-year timestep at each grid box until the end year of the ensemble is reached (usually 2100, so the 1950–2100 trend is the last one to be calculated). We use the ordinary least squares method to compute the trends. Figure 1(a) illustrates the noise in CESM2-LE for an SSS trend spanning 1950–2020, while figure 1(b) shows the SNR in the same ensemble at year 2025. As discussed below, these definitions of noise and SNR are physically meaningful, supporting the use of this methodology for assessing changes in SSS across multiple LEs.

As noted in previous work (Schlunegger *et al* 2020), ToE is a convenient metric for normalizing results across different types of ESMs, different emissions scenarios, and different physical variables. It can inform the design and analysis of the observing network by defining the temporal and spatial scales required for monitoring significant change. Although it has been discussed as a kind of threshold for climate impacts on marine organisms and ecosystems, we note that it is just a statistical metric based on the SNR within the models' worlds, not the real world. An SNR of less than two does not necessarily mean that no impacts of the forced response are occurring over the given time period.

The applicability of ToE to the real world is limited by the assumption that the ESMs simulate the correct patterns and magnitude of internal variability, and produce the correct forced response. We perform a basic model evaluation to establish their credibility, but our goal is not to constrain projections based on the 'best' model or set of models. Rather, the systematic model intercomparison and model-observational comparison presented here is intended to highlight the most common (and likely observable) signals of ocean surface change and their relative timing across different regions. The evaluation also aids in the interpretation of the SSS trend as an amplification of its climatological pattern. An advantage of LEs over smaller ensembles is that these climatological patterns, and their biases relative to observations, are very robust due to the large sample size. While the ToE patterns are suggestive of underlying physical processes that we discuss, it is beyond the scope of this work to conduct a detailed process-based analysis.

2.4. Other methods and datasets

Ordinary least-squares linear trend analysis is used to evaluate observed and modeled patterns of ocean surface change. A two-sided Student's t test is applied to determine whether the trends are statistically significant at the 95% confidence level or higher. We measure the similarity between two patterns using the pattern correlation statistic, r. The pattern correlation is the *Pearson* correlation coefficient between two maps, for example, the observed SSS climatology and the SSS climatology simulated by a model. It applies a cosine of latitude weighting to account for differences in the area represented by each grid box value. To explore the role of the global mean, we consider both the centered (means of the compared fields removed) and uncentered (means of the compared fields not removed) pattern correlations, and report which was used in the text or figure captions. This choice tends to make little difference for the global pattern correlations when two fields of the same variable are compared (such as a simulated trend versus an observed trend), but can make a difference within an ocean basin. When two dissimilar quantities are compared, such as the trend pattern versus the climatological pattern, we find that the centered pattern correlation gives the best results.

To connect SSS change with the intensification of the hydrologic cycle, we adopt the GSSSC index of Douville and Cheng (2024). As a timeseries, the GSSSC index provides a simple way of gauging the 'fresh get fresher, salty get saltier' pattern in models and observations, while also serving as a metric for model evaluation. To calculate the index, we use the simplest method described in Douville and Cheng (2024), in which the fixed, annual-mean E–P field differentiates the fresh and the salty areas for all time steps. Area weighting is applied as described above. The GSSSC is simply the salinity averaged across evaporation-dominated regions minus salinity averaged across precipitation-dominated regions. It differs from the SC index of Cheng *et al* (2020) in that it uses E–P to delineate these regions rather than the salinity field itself, thus linking the salinity change directly to the process that it is thought to be most relevant for those changes. Unlike SC, GSSSC does not use an absolute salinity value to separate fresh and salty regions, thus avoiding model biases in climatological salinity. We also compute an ad hoc index which connects the evolving SSS signal from the ToE calculation to the SSS climatology using pattern correlation. To facilitate these last parts of our analyses, we utilize the ERSSTv5 SST reconstruction (Huang *et al* 2017), as well as the E–P climatology from the ERA5 reanalysis (Hersbach *et al* 2020).

3. Results

3.1. Climatology and noise of SSS

We begin with the climatology (also called the 'mean state') for three main reasons. First, it highlights the degree of consistency across observational data products and helps to build an intuitive understanding of what processes control the SSS field. Second, it helps to establish the credibility of the models used to make projections of ocean surface change. Third, because the forced SSS trend is often characterized as an amplification of the climatological patterns (e.g. Durack *et al* 2012, Cheng *et al* 2020, Douville and Cheng 2024), it defines a baseline against which to measure the pattern amplification.

The observed climatology in OISSSv2 (figure 2(a)) is characterized by an inter-basin contrast between the salty Atlantic and the relatively fresh Pacific. Meridional contrasts between the subtropical dry zones and the tropical convergence zones are evident in both the Pacific and Atlantic. The Arctic is the freshest region on the globe, but the relatively fresh Southern Ocean occupies a larger area. These patterns generally correspond with the mean state E–P field, which is contoured from ERA5 in figure 2(a) and displayed for model output in figure 2(d). Due to ocean surface currents and vertical mixing, the salinity contrasts are muted compared with the E–P contrasts (e.g. Terray *et al* 2012). The Norwegian Sea, a relatively salty region at the northern terminus of the Gulf Stream where precipitation exceeds evaporation, shows clear evidence of ocean circulation's influence. The Indonesian throughflow current, transporting relatively fresh waters

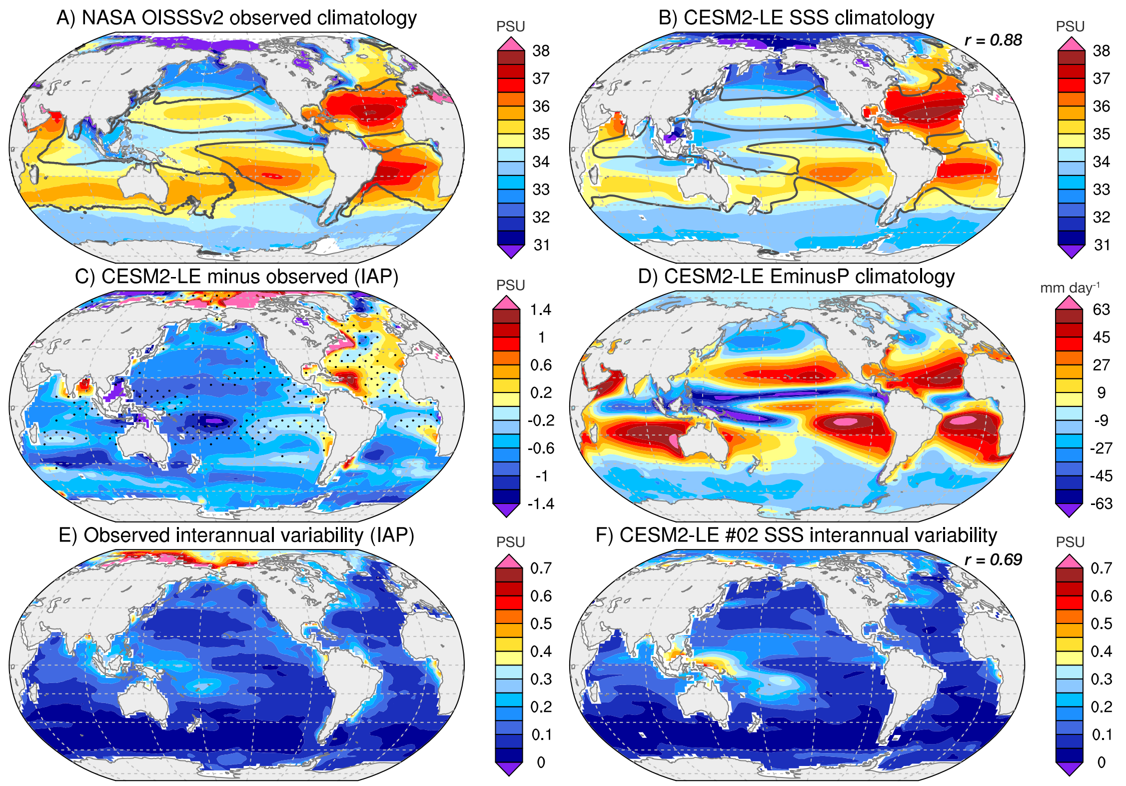

Figure 2. Annual-mean climatology in observations and CESM2. (a) SSS climatology (2012–2023) in OISSSv2. The heavy gray contour lines denote where annual *E–P* equals zero in the ERA5 data during 1951–2000; (b) SSS climatology (1951–2000) in CESM2-LE ensemble mean, indicating the centered pattern correlation, *r*, against observations over 40° N to 40° S. The heavy gray contour lines denote where annual *E–P* equals zero in the CESM2-LE ensemble mean during 1951–2000; (c) Model-observational SSS difference (CESM2-LE 1951–2000 minus IAP 1951–2000). Stippling indicates areas where the model-observational difference is less than the magnitude of the ensemble spread; (d) climatology (1951–2000) of *E–P* in CESM2-LE ensemble mean; (e) interannual variability (standard deviation of the annual mean) in the observational IAP dataset (1951–2000); (f) interannual variability in member 2 of CESM2-LE (1951–2000), indicating the centered pattern correlation, *r*, against the observed variability pattern over 40° N to 40° S (note the uncentered correlation is higher at $r = 0.91$).

westward from the wet western tropical Pacific, likely contributes to the sharp contrasts in salinity on either side of the Indian subcontinent. The Kuroshio current transports relatively fresh tropical water along the eastern coast of Asia, across the subtropical dry region. In the Southern Ocean, the non-zonal path of the Antarctic Circumpolar Current is evident in the contrast between the relatively fresh polar waters and the saltier mid-latitudes. As shown in figure S1, the global SSS pattern is very similar in the IAP dataset. In absolute terms, the IAP dataset is slightly saltier than OISSSv2 (figure S1(f)), but largely within the reported 0.2 practical salinity unit (PSU) uncertainty of OISSSv2 (Melnichenko *et al* 2021).

The four LEs evaluated here all exhibit high pattern correlations with the observed SSS climatology (figures 2 and S2–S4), with CESM2, shown in figure 2(b), leading the group. For brevity, we focus on CESM2. The climatologies and bias patterns of the other three LEs are shown in figures S2–S4. Globally, CESM2's SSS pattern (figure 2(b)) broadly corresponds with the *E–P* field (figure 2(d)), but the gradients in *E–P* are sharper than those in salinity. CESM2 has a fresh bias across most of the global ocean, with the exceptions of the North Atlantic and central Arctic (figure 2(c)). Note that in many areas, indicated by stippling in figure 2(c), the bias of the ensemble mean is smaller than the ensemble spread, and it is smaller than one PSU across the majority of the domain. A prominent region of high saline bias occurs along the northeastern U.S. and Canadian Atlantic coast, likely due to the too-far-north separation of the Gulf Stream from the continental shelf in CESM2 (Danabasoglu *et al* 2020). Due to limited polar observations and seasonal sea ice cover, we do not place much importance on the CESM2's bias pattern in the central Arctic, but this could be associated with the model's too-thin sea ice (DeRepentigny *et al* 2020). The generally too-fresh bias pattern, and the broad correspondence between SSS and *E–P*, are shared among the models (figures S2–S4); note that the models would appear slightly less fresh biased if compared with OISSSv2. MPI-ESM (figure S3(c)) is notable for its lack of a saline bias in the north Atlantic. It is also notable for the large areas where the ensemble spread exceeds the magnitude of the bias in the ensemble mean, but this likely stems from variability that is larger than observed across many areas of the global ocean (figures S3(e) and (f)).

The observed interannual variability of SSS (figure 2(e)) exhibits its own unique pattern, with the rainiest areas in the western tropical Pacific, intertropical convergence zone (ITCZ) and South Pacific convergence zone (SPCZ) having the highest variability, consistent with rainfall in these regions being convective in nature and strongly influenced by ENSO and Pacific decadal variability (e.g. Capotondi *et al* 2020). This SSS variability may not only be due to local rainfall variability, but also due to interannual variations in inter-basin moisture transport. For example, moisture transport from the Indian to Pacific basin associated with the southeast Asian monsoon is one of the key processes for the Pacific to maintain its freshness (Craig *et al* 2023). This transport has strong seasonality and strong interannual variability. Other areas of relatively high variability include the Kuroshio Extension and Gulf Stream separation regions, as well as the margins of the Arctic Ocean. The lowest variability occurs in the Southern Ocean. The models are worse at simulating the interannual variability pattern than they are at simulating the climatology, but CESM2 also leads the group in this pattern correlation metric (figures 2(f), S2(f), S3(f) and S4(f)), exhibiting both the individual member with the highest pattern correlation and the highest average pattern correlation across its ensemble members (figure 1(c)). However, in CESM2 the SSS variance in the western Pacific appears to be too large, perhaps associated with the model's too-large ENSO amplitude, too-far-west displacement of ENSO-related anomalies (Capotondi *et al* 2020) and too-strong SPCZ (Wei *et al* 2021).

The pattern of variability averaged across all members of CESM2-LE (figure 1(c)) is broadly consistent with the noise pattern as defined in the ToE analysis (figure 1(a)). Tropical regions dominated by convective precipitation are the noisiest, especially in the western Pacific warm pool, the SPCZ, and the Asian monsoon region. Other areas of relatively high noise include the Kuroshio Extension and Gulf Stream separation regions, where fresh subpolar waters mix with saltier mid-latitude waters. The margins of the Arctic Ocean are nosier than the central Arctic, perhaps due to variability in river runoff and seasonal ice cover. The Pacific ITCZ exhibits a moderate amount of noise, while the least noise is found across the Southern Ocean, the relatively cold southeastern tropical Pacific, and the north Pacific and north Atlantic mid-latitude storm track regions. Overall, the Pacific and Indian oceans are noisier than the Atlantic and Southern oceans.

3.2. Historical trends of SSS

Having established that the models provide credible simulations of the SSS climatology and SSS variability, we now turn to their simulations of historical trends. The observed trend over 1950–2021 (figure 3(a)) features significant freshening in the Arctic, north Pacific, ITCZ, western tropical Pacific and the Pacific sector of the Southern Ocean. Salting trends occur across the Atlantic between 40° N and 40° S, and in the southeastern subtropical Pacific. The trend in the CESM2-LE ensemble mean, shown in figure 3(b), generally agrees in sign with the observed trend in the Arctic, Atlantic, and north Pacific, but the near-global centered pattern correlation is only 0.4. CESM2-GHG (figure 3(c)) shows a considerably higher pattern correlation of 0.54, much higher than any all-forcing, ensemble-mean trends (ranging from $r = 0.14$ for MPI-ESM to $r = 0.4$ for CESM1-LE and CESM2-LE). Figure S5 displays the centered and uncentered pattern correlations across all ensemble members of the seven ensembles for the global, Pacific, and Atlantic domains. Clear structural differences among the models are evident, as well as sensitivity to external forcing and considerable spread due to internal variability. The uncentered correlations give the clearest results for the subdomains.

Although its trend magnitudes are often higher than observed, in addition to the Arctic and Atlantic trends, CESM2-GHG captures well the freshening trend in the western tropical Pacific, and the salting trends in the eastern subtropical Pacific dry zones. This suggests that the observed trend pattern is consistent with the forced response to GHGs, while the additional (non-GHG) forcings applied in CESM2-LE tend to degrade the consistency of the simulated and observed trends. In the tropical and subtropical Pacific, the SSS pattern in CESM2-LE (figure 3(b)) resembles the second aerosol-driven pattern identified by Dong *et al* (2024; their figure 2(j)), which strengthens from 1950 to 2020, in line with the trend period analyzed here. The first (and more dominant) aerosol-driven pattern identified Dong *et al* (2024; their figure 2(f)) is opposite in sign to the GHG-driven pattern in the northern hemisphere, and has little effect in the southern hemisphere. As such, aerosols can explain why the SSS signal in CESM2-LE is muted compared with the SSS signal in CESM2-GHG, as well as why the tropical and subtropical Pacific signals are different. From the set of experiments in table 1, the most direct way to estimate the role of aerosols on these trends is from the difference of CESM1-LE and CESM1-xAER. As diagnosed in figure S6, aerosols drive a roughly opposite trend pattern to GHGs, muting the all-forcings forced response.

We next use the ensembles to examine the role of internal variability in the SSS trend pattern. The SSS trend in the second ensemble member of CESM2-GHG (figure 3(d)) exhibits the highest pattern correlation with the observed trend of any ensemble member of the ensembles listed in table 1 (215 individual members; see figure S5(A)). Unlike the ensemble mean, member 2 has an asymmetric salinity trend across the equator, with greater freshening north of the equator, similar to the observed trend. This corresponds with an increase in tropical Pacific rainfall in a pattern suggesting an intensification of the ITCZ (figure 3(e)), which resembles

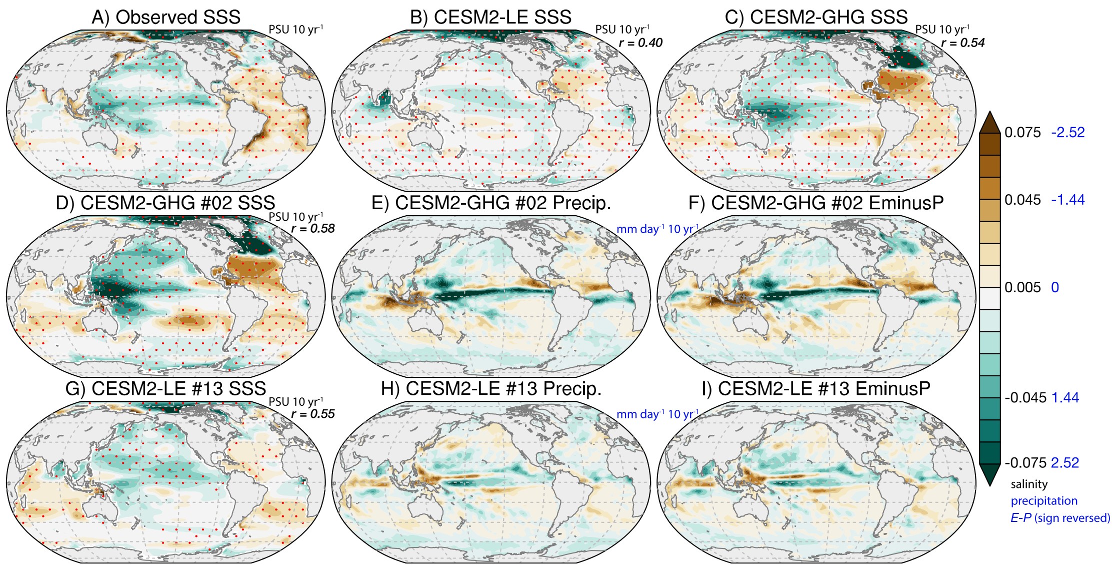

Figure 3. Historical (1950–2021) decadal trends in annual-mean SSS and related variables. (a) Observed SSS trend in the IAP dataset; (b) SSS trend in CESM2-LE ensemble mean; (c) SSS trend in CESM2-GHG ensemble mean; (d) SSS trend in CESM2-GHG member 2; (e) precipitation trend in CESM2-GHG member 2; (f) *E–P* trend in CESM2-GHG member 2; (g) SSS trend in CESM2-LE member 13; (h) precipitation trend in CESM2-LE member 13; (i) *E–P* trend in CESM2-LE member 13. For the SSS trends, red stippling indicates statistical significance at the 95% confidence level according to a two-tailed *t-test*. Also indicated for the modeled SSS trends are their centered pattern correlations, *r*, against the observed trend pattern over 40° N to 40° S. See figure S5 for a summary of pattern correlation statistics. Note that the precipitation and *E–P* trends share the same scale, but the sign of *E–P* is inverted.

observed rainfall trends (e.g. Wodzicki and Rapp 2016). In the tropical Pacific, the *E–P* trend pattern (figure 3(f)) is dominated by the rainfall trend. Thus, assuming no significant changes in ocean circulation, we infer that the tropical Pacific rainfall trend is the primary driver of the tropical Pacific SSS trend.

In the north Atlantic, internal variability appears to be less relevant than in the Pacific, as there is not much difference between the ensemble-mean trend and the trend in member 2. We have also seen above that the magnitude of interannual variability is smaller in the Atlantic. (see figures 2(e) and (f)). Furthermore, there is a small ensemble spread in the uncentered pattern correlations between observed and simulated trends in the Atlantic basin in CESM2-GHG (figure S5(c)). In member 2, evaporation trends contribute to the *E–P* trend, such that there is a meridional dipole in *E–P* (figure 3(f)) that corresponds with the meridional dipole in SSS (figure 3(d)). However, we cannot ignore the roles of other processes. In the Arctic, the freshening trend is consistent in sign with increased precipitation (figure 3(e)), but this precipitation trend is small. It is likely that sea ice loss (which is simulated in CESM2 historical simulations, DeRepentigny *et al* 2020) contributes to the Arctic freshening signal, which in turn contributes to the weakening of the AMOC in CESM2-GHG (Simpson *et al* 2023). This would trigger a positive feedback in which decline of northward salinity transport by the AMOC will further weaken the AMOC, amplifying the north Atlantic salinity dipole trend pattern. This feedback could be partly counteracted by the increasing salinity in the southeastern north Atlantic (10° N to 40° N) as well as the need for the AMOC to balance upwelling elsewhere in the global ocean (e.g. Baker *et al* 2025).

In comparison to the CESM2-GHG ensemble, the CESM2-LE ensemble on average does worse at replicating the observed SSS trend pattern in the tropical and subtropical Pacific (figure S5(b)). However, the role of internal variability in the Pacific is underscored by the fact that some ensemble members can exhibit pattern correlations as high as $r = 0.6$. The highest correlating member globally, member 13, shows a general Atlantic salting and Pacific and Arctic freshening similar to observed, but does not capture the details of these patterns (figure 3(g)). It also does not produce realistic looking tropical rainfall (figure 3(h)) and *E–P* trends (figure 3(i)) in the tropical Pacific. Together, these results suggest that the observed trend is best explained by a combination of the forced response to GHGs and internal variability. This assessment is supported by the fact that MIROC6-GHG exhibits similarly high pattern correlations as CESM2-GHG, while CESM1-xGHG (where GHG concentrations are held constant) has low, slightly negative pattern correlations (figure S5(a)). While other forcings present in CESM2-LE, particularly aerosols, strongly influence the simulated historical SSS trend pattern (Dong *et al* 2024), there are large uncertainties in the modeling of aerosols and aerosol-cloud interactions (e.g. Simpson *et al* 2023). We will return to the interpretation of the historical trend patterns below. The important point here is that the models, especially CESM2, are capable of

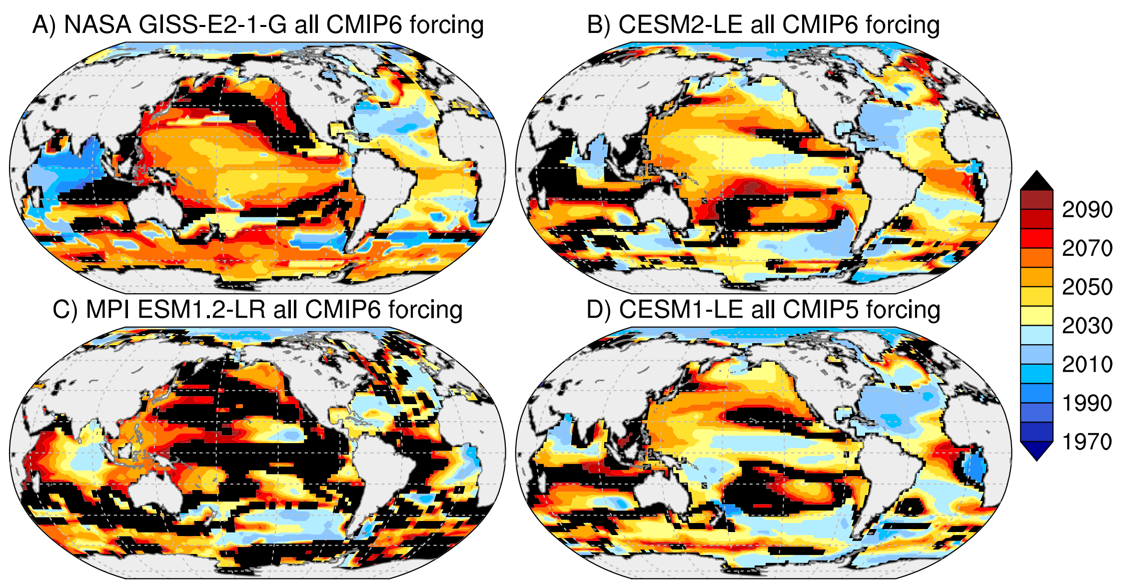

Figure 4. Time of emergence of the annual-mean SSS signal (ensemble-mean trend starting in 1950) in four, all-forcing initial condition LEs: (a) NASS GISS E2-1-G; (b) CESM2-LE; (c) MPI-ESM 1.2-LR; (d) CESM1-LE. Areas filled in black do not emerge by 2100, the end of the experiments. Note that blue areas have emerged within the historical period (by ∼2025).

producing credible simulations of the long-term historical trend on global and basin-wide scales, suggesting that they are fit for the purpose of estimating ToE, which we examine next. On the other hand, the models are not equal in their skill at replicating observed trends (figures S5(a) and (b)), which is an important context for the following results.

3.3. ToE

Figure 4 presents ToE for SSS in the four models for trends starting in 1950. CESM2 (figure 4(b)) and CESM1 (figure 4(d)) show the earliest global-average ToE, with average emergence years of 2044 and 2043 when considering those grid boxes that emerge by 2100. The MPI-ESM (figure 4(c)) has an average year of emergence of 2052 (not counting grid boxes that show no emergence by 2100). GISS-E2-1-G (figure 4(a)) shows strong contrasts between adjacent regions, for instance emerging by ∼1990 in the Indian Ocean, but not until the late 21st Century in the western tropical Pacific. These differences notwithstanding, there are broad similarities among the ToE patterns. The Arctic emerges around 1990 or 2000 in all models, followed by the subtropical and mid-latitude north Atlantic in the 2010s. The southeastern Pacific emerges in the 2010s or 2020s in three of the four models, and as early as the 1990s in GISS-E2-1-G. For CESM2-LE, the ToE pattern (figure 4(b)) closely corresponds with the SNR pattern (figure 1(b)). By definition, this is true for each of the models (not shown).

All models show at least a small patch of early emergence in the Indian Ocean, but there is not agreement on its location. This is likely due to uncertainty in the aerosol forcing, which drove strong salinity trends in the mid-20th Century (Dong *et al* 2024). The aerosol signal appears to be especially prominent in GISS-E2-1-G, in which a broad area of the Indian Ocean emerges in the 1980s or 1990s. If 1990 is used as the start date for the trends instead of 1950, then the signal does not emerge by 2100 across most of the Indian Ocean in GISS-E2-1-G (not shown). In CESM1, aerosols cause strong salting across the Bay of Bengal and South China Sea during 1950–2021 (figure S6(c)).

There is a clear pattern in both CESM models and GISS-E2-1-G of the central and eastern tropical Pacific emerging sooner than the subtropical dry zones and western tropical Pacific. The dry zones (where $E > P$ on figure 1(b)) are generally home to weak salting trends (e.g. Figures 3(a)–(c)), even in the future under strong, GHG-only forcing (figure S7(b)). The western Pacific has a strong freshening signal (e.g. Figures 3(a)–(c); S6(a) and (b)), but the noise is relatively large here (e.g. figure 1(a)). The central tropical Pacific has a persistent freshening signal and relatively low noise. Considering these characteristics of signal and noise, we can appreciate why the signal in the central tropical Pacific emerges sooner than in the subtropical and western tropical Pacific, in all models except for MPI-ESM (figure 4(c)).

Figure 5(a) summarizes the ToE results by showing the earliest decade of emergence among the four LEs. It displays a clear pattern of early emergence in the Arctic, southwestern north Atlantic, and southeastern Pacific, with additional regions in the northeastern Pacific and central tropical Pacific also emerging within the historical period. As noted above, the Indian Ocean is an outlier in the GISS-E2-I-G model, so we do not

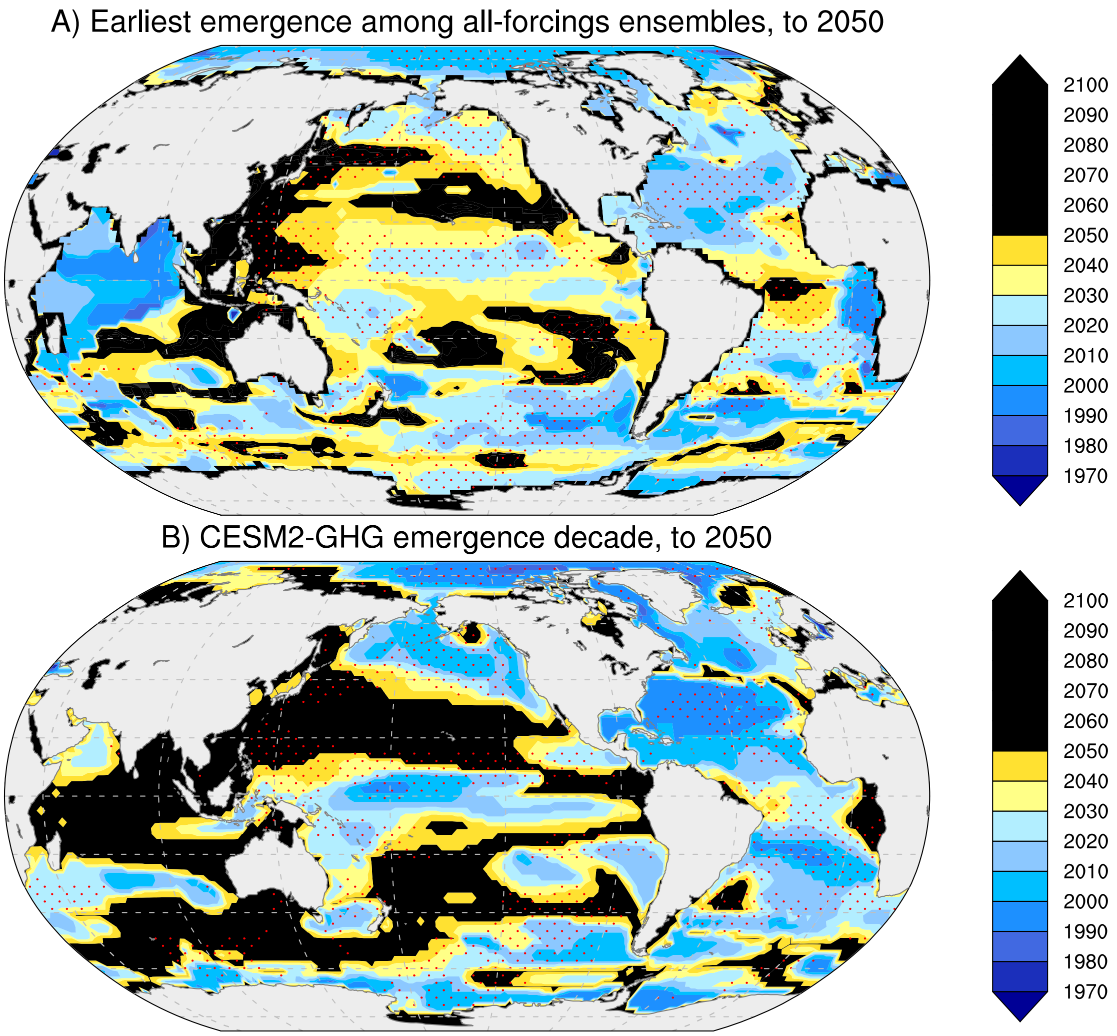

Figure 5. (a) The earliest decade of emergence among the four LEs from figure 3; (b) SSS time of emergence in the CESM2-GHG ensemble. Areas filled in black do not emerge by 2050, the end of the CESM2-GHG experiment. For consistency, panel A only shows pre-2050 emergence. For both panels, red stippling indicates where a significant observed trend exists, as shown in figure 2(a). Note that blue areas have emerged within the historical period (by ∼2025) according to the models.

include it in our description of the historical emergence pattern. Emerging in the second half of the 21st Century are vast regions of the subtropical and mid-latitude Pacific, western Pacific, and equatorial Atlantic. Superimposed on this map are markers indicating where the observed historical trend (1950–2021; figure 3(a)) is statistically significant. The degree of overlap is striking—the blue areas of historical signal emergence in the models lines up with significant observed trends. However, the observations show significant trends in the western tropical Pacific and tropical Atlantic, two regions where the models project a mid-to-late 21st Century emergence. These are areas of large interannual variability—perhaps a little too large in the models as compared to observations in the western Pacific (figures S2–S4) Despite the models' agreement with observations on the sign of change, the SNR is not large enough to satisfy the ToE definition with the historical period (see figure 1(b) for SNR in CESM2-LE). The SNR also is not large enough in the Indian Ocean and subtropical Pacific, regions where observed trends are generally weak and not significant.

3.4. Drivers of the ToE pattern

The role of GHGs in shaping the ToE pattern in SSS is illustrated in figure 5(b), which shows the ToE for CESM2-GHG. It mirrors the multi-model consensus pattern in figure 5(a) in that it shows the earliest emergence in the Arctic and southwestern north Atlantic, and the latest emergence across the subtropical and mid-latitude Pacific. Compared to all forcings, GHGs drive historical emergence across an even greater portion of the Atlantic basin, including the tropical Atlantic, where the observed trends are significant. GHGs also drive historical emergence across a larger area of the central-western tropical Pacific, in the northeastern Pacific near Alaska, and in the southeastern Pacific off the coast of Chile. These are all areas of significant observed trends. Most areas of insignificant observed trends are also areas where CESM2-GHG

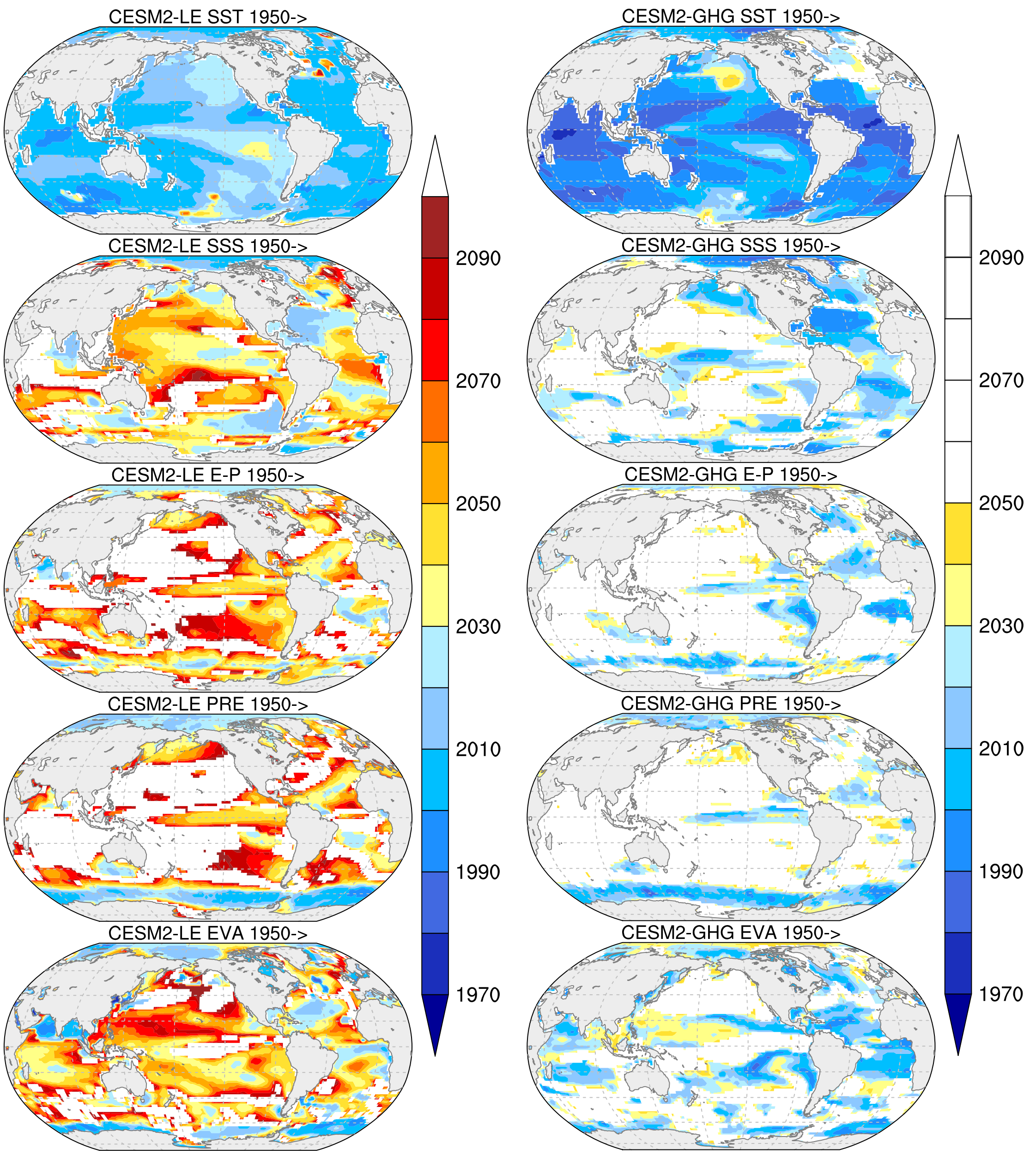

Figure 6. (left column): Time of emergence for all examined fields in CESM2-LE. White areas do not emerge by 2100. (right column): time of emergence for all examined fields in CESM2-GHG. White areas do not emerge by 2050.

does not project historical emergence. Overall, the other single-forcing LEs exhibit similar GHG-driven ToE patterns (figure S8), with historical emergence in the Arctic, Atlantic, and parts of the Southern Ocean featured in all three models. They also agree that the Indian Ocean signal does not emerge until after 2050 if at all in the 21st Century (though only one of the single-forcing LEs, MIROC6-GHG, extends to 2100, and it follows a low-emissions scenario).

We examine the correspondence between the ToE pattern in SSS and the corresponding ToE patterns in *E–P*, precipitation, evaporation, and SST, for both CESM2-LE and CESM2-GHG (figure 6), as well as the underlying trends in these variables over 1951–2050 (figure 7). SST (figure 6, top row) largely emerges before SSS (figure 6, second row), except in the north Atlantic north of ∼40° N. *E–P* (figure 6, third row) emerges during the historical period in the polar regions, and earlier in the Atlantic than in the Pacific, broadly similar to the salinity pattern. *E–P* signals also emerge sooner in the eastern than western Pacific, again consistent with the salinity emergence pattern. Precipitation signals (figure 6, fourth row) emerge first in the polar regions, and then in the subtropical Atlantic and eastern tropical Pacific. Evaporation signals (figure 6, fifth row) have more of a polar and subtropical signature, with Atlantic subtropical evaporation signals generally emerging sooner and across a wider area than their Pacific counterparts.

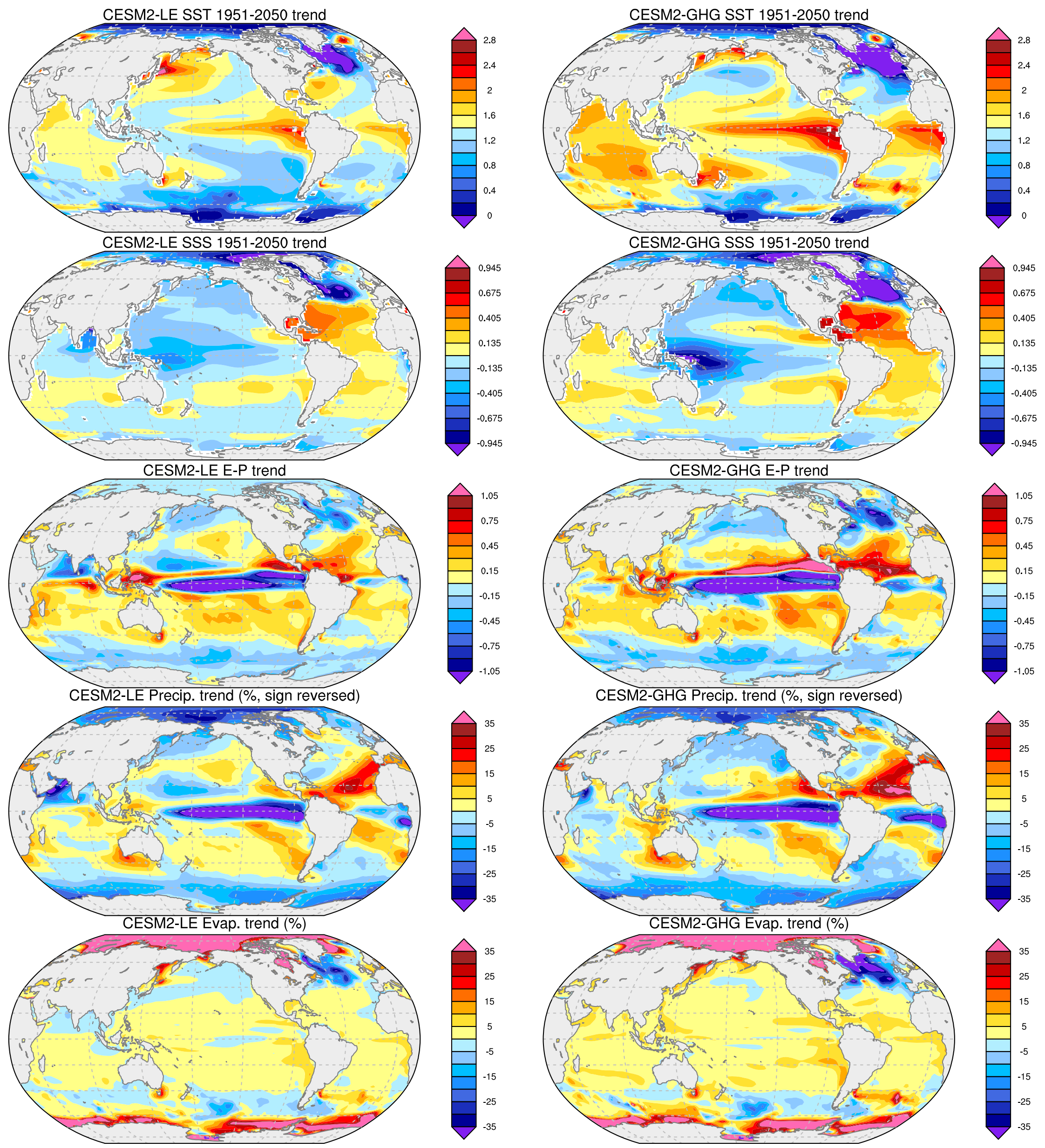

Figure 7. Trends (epoch differences of 2041–2050 minus 1951–1960) in all examined fields in CESM2-LE (left column) and CESM2-GHG (right column), corresponding with the ToE maps in figure S8. Note that the precipitation and evaporation trends are given as percent changes, E–P as mm d^{-1}, SSS as PSU yr^{-1} and SST as °C yr^{-1}.

The trends during 1951–2050 in these physical variables (figure 7) are suggestive of tight linkages between SST, E–P and SSS. Warming trends are maximized in the eastern equatorial Pacific and to some extent in the equatorial Atlantic (figure 7, top row). Increases in precipitation are also maximized along these equatorial bands, which are flanked by drying trends in the subtropics (figure 7, fourth row). The polar regions also see relatively large increases in precipitation, partly counteracted by increases in evaporation (figure 7, bottom row). The E–P signal is maximized in the tropics and northern subtropics (figure 7, third row). The SSS trend pattern (figure 7, second row) can be characterized as an attenuated version of the E–P trend pattern. Transports by the wind-driven ocean circulation in both the Atlantic and Pacific may explain why the maximum SSS trends are shifted west from the maximum E–P trends (Lu *et al* 2024). In addition to this, we note that the depth-integrated climatology of the Pacific is fresh, even in the evaporation-dominated subtropics (Cheng *et al* 2020). Thus, the surface salting signals tend to be attenuated by vertical mixing contributing to the late emergence of those signals. By contrast, the subtropical North Atlantic is salty over 0–2000 m depth, so vertical mixing is less able to attenuate the surface signal from E–P.

To completely describe the SSS trend, the role of heat fluxes associated with the SST trends must be considered, as warming generally leads to a decrease in surface density (e.g. Lu *et al* 2024). In the idealized experiments of Lu *et al* (2024) and Zhu and Liu (2020), heat fluxes are the primary cause of AMOC weakening, which contributes to increases in salinity south of ∼40° N and freshening north of 40° N. Neither of these studies evaluated the role of the cryosphere on SSS trends, however other experiments have shown that Arctic sea ice loss leads to a gradual freshening of the Arctic and north Atlantic (Li and Fedorov 2021). In summary, ocean surface warming, which emerges first (figure 6), sets the stage for the emergence of the SSS trend in at least three ways. First, warming focused at the equator shifts rainfall patterns towards the equator, at the expense of drying in the subtropics, as part of the overall intensification of *E*–*P* fluxes. Second, warming-driven changes in ocean surface density lead to changes in water mass formation with consequences for the salinity distribution (Silvy *et al* 2020, Lu *et al* 2024). Third, warming causes sea ice loss and ice sheet melt, which freshen and stratify the surface ocean (e.g. Sadai *et al* 2020, Li and Fedorov 2021). Finally, a recent study (Li and Liu 2025) evaluates realistic CMIP5 and CMIP6 historical experiments like the ones considered here to argue that the AMOC has in fact been weakening during the historical period, contributing to the observed SSS trend pattern in the Atlantic and the Arctic.

We now turn to a more direct way of linking SSS trends with *E*–*P* trends. The GSSSC index, measuring the divergent salinity trends between climatologically wet and dry areas and shown in figure 8(a), steadily increases between 1950 and 2100 in all experiments. The 1950–1980 value of ∼1.5 psu in the observations is best captured by the CESM2-LE and GISS-E2-1-G, while the trend is best captured in CESM2-LE. The GSSSC accelerates too rapidly in CESM2-GHG compared with the observed rate, reinforcing the impression from the trend map in figure 3(c) that the GHG-only salinity trends are too strong. In all models, the GSSSC increase is driven more by freshening (figure S9(b)) than by salting (figure S9(c)), in agreement with Douville and Cheng (2024). However, in the Atlantic, there is more of a balance between freshening trends (figure S9(e)) and salting trends (figure S9(f)). The global mean is dominated by the Pacific due to its larger area. In short, these results affirm the 'fresh get fresher, salty get saltier' paradigm, but suggest that it is not universal within all ocean basins.

Is the SSS signal an amplification of the climatological salinity pattern? While the GSSSC index partly addresses this question, we examine it directly by correlating the evolving signal from the ToE analysis (i.e. the ensemble-mean trend in 5 year increments since 1950) with the SSS climatology (i.e. the patterns shown in figures 2(b), S2(b), S3(b) and S4(b)). As shown in figure 8(b), the SSS climatological patterns amplify in all models and in the observations. The observed amplification is evident around 1990, reaching $r = 0.3$ by 2020. CESM2-LE is the closest to this value at 2020. Prior to 1980, all the models have a declining or even negative pattern correlation, consistent with the aerosol-induced SSS patterns discussed by Dong *et al* (2024) and displayed in figure S6. This anti-correlation is absent in CESM2-GHG, making it clear that it cannot be due to GHGs. The fact that the all-forcings LEs all have it to some degree makes it clear that it is not due to internal variability. Another interesting feature of the pattern evolution is that once that pattern establishes itself, it does not change further—the pattern correlation plateaus at a value around $r = 0.6$. This does not mean that freshening and salting trends (figure S9) will not continue to intensify; it simply means that the spatial pattern of those trends will not significantly shift.

The ensemble spreads of the trend-mean state pattern correlations at present day are shown in figure S10, broken down into global, Atlantic, and Pacific domains. This reinforces three messages from the above results: First, the pattern amplification is stronger in the Atlantic than in the Pacific Second, internal variability can strengthen or weaken the pattern amplification, but it does not fundamentally obscure the signal of the forced response on the global scale. Third, the pattern amplification is largely driven by GHGs. The GHG-only experiments, CESM2-GHG and MIROC6-GHG have the highest average positive pattern correlations, while the experiment with fixed GHG concentrations, CESM1-xGHG, has weak or strongly negative pattern correlations.

The results in figure 8(c) confirm that the SSS pattern amplification is warming-driven. Here, the *x*-axis is the SST change since 1950 in the given model rather than the end date of the trend signal. This effectively collapses the curves from figure 8(b). These results suggest that the sensitivity of the SSS pattern amplification to warming is closest to the observed in CESM2-LE (note the agreement of the black and red curves in figure 8(c)). However, the anti-correlation due to aerosols in both versions of CESM appears to be overdone. The observations show only a weak anti-correlation to the mean state before the pattern begins to amplify. Under GHG forcing only, the pattern amplifies too soon (yellow curve in figure 8(c)). Aerosols are important for delaying this amplification but may not be correctly modeled. Recent studies have highlighted the models' inability to simulate historical SST trend patterns even if internal variability is taken into account (Wills *et al* 2022). These historical SST trend patterns, which are not explained by aerosols, dampen the warming signal (Armour *et al* 2024), which in turn would dampen the SSS signal.

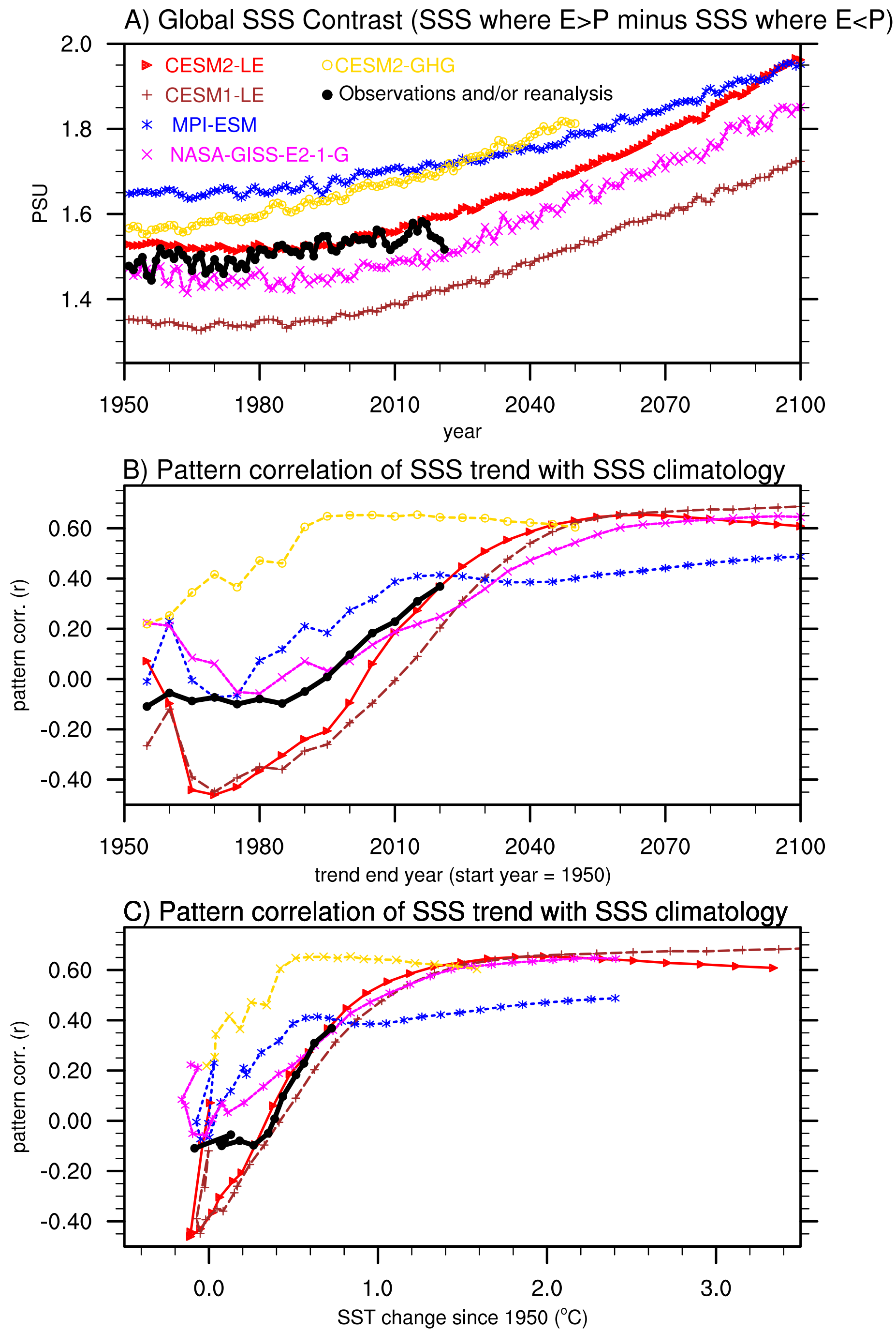

Figure 8. (a) The global SSS contrast (GSSSC) index after Douville and Cheng (2024) using a simple static definition of annual-mean *E–P*; (b) The evolving centered pattern correlation of the SSS trend (with a start date of 1950) with the SSS climatology (1951–2000) over domain of 40° N to 40° S; (c) As in (b), but the *x*-axis is the global SST change since 1950 corresponding to the year when the given pattern correlation occurs. ERSSTv5 is used as the observational SST dataset, while ERA5 is used to estimate the observational *E–P* field.

4. Discussion and conclusions

Leveraging state-of-the-art observational datasets and Earth System Models, we have evaluated the ToE of forced SSS change and gained new insights into the drivers of this change. The consensus of the four LEs evaluated here is that the SSS signal first emerges (in the 1990s and 2000s) in the Arctic and southeastern north Atlantic, with the south Atlantic and parts of the Southern Ocean close behind, emerging within the historical period. Most of the Pacific signal emerges in the second half of the 21st Century. It is not clear if signals should be expected to emerge at all during the 21st Century across much of the Indian Ocean due to model disagreement. The broad pattern of these results can be understood simply: The polar regions and the Atlantic basin have more drivers of the signal (including *E–P*, AMOC slowdown, and sea ice melt), and the

Pacific and Indian oceans have more noise (figure 1(a)) with less influence on the signal from processes besides changes in *E–P* and the direct impacts of ocean surface warming. In the Arctic and north Atlantic in particular, all of the major processes—*E–P*, AMOC slowdown, and sea ice melt—contribute to freshening north of ∼40° N and salting south of ∼40° N.

To understand the drivers of the signal emergence and the credibility of the models, we compared the SSS trend patterns simulated by the models to long-term (72 year) trends in the IAP dataset. We also considered LEs forced by GHGs alone. The observed trend pattern features freshening in the Arctic, north Atlantic, western tropical Pacific and Pacific ITCZ, Pacific sector of the Southern Ocean, and in the northeast Pacific. Salting trends occur in the Atlantic basin between 40° N and 40° S, and in the eastern subtropical Pacific. This pattern involves a growing SC between the salty Atlantic and fresh Pacific (similar to Douville and Cheng 2024). In our pattern correlation analysis, the observed global trend pattern is best explained by the forced response to GHGs, plus a component of internal variability that is important for the asymmetric freshening trends in the central and western tropical Pacific, which are more pronounced north of the equator. Nonetheless, the MIROC6 model suggests that freshening trends focused north of the equator in the eastern Pacific could be a response to GHGs alone (figure S7(c)). Overall, MIROC6 scores similarly to CESM2-GHG in simulating the historical trend pattern in the Pacific (figure S5(b)).

In the all-forcings LEs (particularly CESM2-LE), it appears that the dynamic response to aerosol distributions—the second aerosol mode discussed in Dong *et al* (2024)—degrades the fit of the forced response and the observed trends, especially in the tropical Pacific. Nonetheless, the primary aerosol-driven signal, which opposes the GHG-driven signal, appears to be important for suppressing the magnitude of simulated SSS trends, and delaying their ToE. The aerosol-induced delay is diagnosed in figure S6(d), showing that the salting trend in the subtropical north Atlantic and freshening trend in the Arctic and north Pacific are delayed by up the three decades. It is an all-forcings ensemble, CESM2-LE, that best matches the observations in terms of the global-scale amplification of the climatological SSS pattern since 1950 (figure 8(c)). Overall, these results confirm the existence of the 'fresh get fresher, salty get saltier' pattern, but this simple view, and its consistent scaling to hydrological cycle intensification, is challenged by the influence of large-scale processes besides local *E–P* fluxes on SSS.

SSS is a powerful climate change indicator, providing complementary information to better-studied and better-observed ocean variables such as SST. We highlight two examples here. First, the north Atlantic is the only region where the SST signal does not emerge by 2050 under GHG-only forcing (figure 6, top row). SSTs in this warming hole region have large interannual to multidecadal variability, yet they have been used to track the AMOC (e.g. Zhu *et al* 2023). As discussed by Zhu and Liu (2020) and Li and Liu (2025), SSS provides an alternative way to track the AMOC's strength. The SSS signal in the south Atlantic, which Zhu *et al* (2023) identify as a fingerprint of AMOC weakening, emerges within the historical period in most of the models evaluated here. The influence of the AMOC on the global SSS signal can be appreciated by comparing the models' SSS trends (figures 3 and S7) to results from the idealized ocean model experiments (using POP2, the oceanic component of CESM1 and CESM2) of Zhu and Liu (2020; their figures 4(b) and (c)). If only *E–P* fluxes drive the SSS signal, then north Atlantic and Arctic SSS trends would be weak, and there would not be a strong contrast in signal strength between the Atlantic and Pacific. If globally uniform ocean-atmosphere heat fluxes act to weaken the AMOC, then a meridional dipole in *E–P* occurs in the north Atlantic, Arctic freshening trends are strong, and the SSS signal is weak outside of the Arctic and the Atlantic. From other work (Simpson *et al* 2023), we know that AMOC weakening starts in the 1980s in CESM2-GHG, while in CESM2-LE, aerosols delay AMOC weakening by a few decades. In addition to the damping impact of aerosols (the first aerosol mode in Dong *et al* (2024)), this can explain the difference in SSS signal strength between CESM2-GHG and CESM2-LE. In summary, AMOC weakening provides a strong signal boost to the forced SSS trends in the Atlantic and the Arctic. Continued SSS observations are critical for monitoring the AMOC and for evaluating which models are providing reliable projections.

SSS observations and observation-model comparisons can shed light on a second challenging problem in modern climate science: The understanding of long-term change in the tropical Pacific. Current-generation models do not reproduce the observed SST or atmospheric circulation trends (Wills *et al* 2022), which play a critical role in the response of the climate system to anthropogenic forcing (e.g. Armour *et al* 2024). Precipitation trends in the tropical Pacific are associated with atmospheric teleconnections that have far-reaching impacts, yet precipitation is a challenging variable to observe and attribute (e.g. Hegerl *et al* 2019). We have shown that salinity changes in the central and western tropical Pacific primarily reflect changes in precipitation (figure 3). By examining these salinity trend patterns, we have identified a potential problem with the dynamical response to aerosols in the models, in that it tends to reduce the consistency of observed and simulated trends in the tropical Pacific. A final interesting aspect of the modeled salinity trends is their east-to-west sequence of the ToE across the tropical Pacific. We tentatively attribute this to three factors: (1) The aerial moisture transport mechanism of Singh *et al* (2016), in which moisture evaporated in the Atlantic over 10° N–20° N is transported by the trade winds to the eastern Pacific with increasing distance as climate warms; (2) The greater noise of SSS in the western Pacific compared to the central and eastern Pacific (e.g. figure 1(a)); and (3) The early emergence of evaporation signals in the eastern parts of the subtropical dry zones (figure 6).

Future work leveraging observations and models is needed to better understand the physical process drivers of both the signal and the noise in the tropical Pacific. In particular, how do ENSO and Pacific decadal variability contribute to the SSS noise in the tropical Pacific, and how well do models represent these processes? How are the observed SST and SSS trends related, and could understanding this relationship help improve the simulation of long-term change in the tropical Pacific? In models, how are the forced responses in SST and SSS related? While recent studies have made some progress in the understanding of tropical Pacific trends and coupled atmosphere-ocean variability, they have largely focused on well-studied variables such as SST, near-surface wind, and sea level pressure (e.g. Wills *et al* 2022, Armour *et al* 2024). The present results suggest that incorporating salinity into this research will provide additional context and insights into mechanisms that are difficult to unravel when studies are restricted to more common variables. Continued SSS observations, whether from reconstructions like the IAP dataset, or from the synthesis of spaceborne observations as in OISSSv2, will be extremely valuable for this work, providing new benchmarks for models and important indications of ocean surface change.

There are several limitations of the present study that may influence the results. First, we have mentioned several model biases in representing the climatological salinity pattern and its variability. These include the fresh bias across much of the global ocean, which has also been found in other recent studies of CMIP6 models (Lu *et al* 2024). Some models, especially MPI-ESM, have very large interannual variability across large areas of the global ocean, while other models, like CESM2, have too much variability in specific areas, notably the western tropical Pacific. These variance patterns have a direct influence on the SNR, which is the core statistic of the ToE metric. Too much noise can delay the ToE. We have also evaluated the signal by comparing the models' forced response patterns (and forced response plus internal variability) to the observed long-term (70+ year) trend patterns. Models have mixed success at reproducing the observed trend pattern, which suggests that their projected future trend patterns may not be accurate. We have evaluated forced responses in a limited number of models, likely not sampling the full range of structural uncertainty among CMIP6 models. Still, there is a diversity of simulated trends across five different models (e.g. figure S5), and yet the models have a consistent sequence of SSS signal emergence, with the Arctic emerging first, followed by the subtropical north Atlantic, the southeastern Pacific, and in some models the central tropical Pacific. The Indian Ocean, western tropical Pacific and subtropical Pacific are slow to emerge in all models (e.g. figures 4 and S8).

While the CMIP6 historical and scenario experiments are often called 'all forcings' experiments, they do not truly include all the forcings, and the responses to some forcings may not be correct. For example, recent studies have highlighted the implications for global climate projections of not including freshwater fluxes from ice sheet retreat (e.g. Sadai *et al* 2020, Schmidt *et al* 2023). Including freshwater fluxes from the Antarctic Ice Sheet can help models better simulate observed tropical Pacific SST trends (Dong *et al* 2022, Armour *et al* 2024) and sea ice trends in the Southern Ocean (Rye *et al* 2020, Roach *et al* 2023). The implication of missing freshwater and other forcing misrepresentation for SSS trends are not fully known and merit further study. Similarly, high resolution ocean and atmospheric modeling has known implications for the simulation of SST trends at least in CESM1 (Yeager *et al* 2023), but the implications of model resolution for the simulation of the salinity signal have not been explored.

Finally, our results highlight that the observed SSS trend pattern is best explained by the forced response to GHGs plus internal variability. This result is best supported by two independently developed models: CESM2 and MIROC6. Consistently, excluding evolving GHG concentrations from the simulation, as in CESM1-xGHG, results in a poor fit to the observed trend pattern. Does this mean that the response to the other major component of anthropogenic forcing, aerosols, is incorrect? We have presented limited evidence that this is the case, specifically highlighting the inconsistency of observed and simulated SSS trend patterns in the tropical Pacific when aerosols are included in the experiment. However, this result is based on analysis of the forced response to aerosols in two closely related models, CESM1 and CESM2 (Dong *et al* 2024), which themselves have differences in how aerosols influence the projection (Simpson *et al* 2023). Moreover, our results also show that GHGs alone overestimate the magnitude of SSS trends, implying that the effect of aerosols on damping the GHG-driven response is necessary for explaining the observations. Evaluating the SSS response to aerosols in single-forcing simulations with additional models should be a priority. We also see value in idealized ocean model experiments, which can be used to isolate the SSS response to specific processes, such as E–P fluxes, heat fluxes, and ice sheet freshwater fluxes. These fluxes can be drawn from historical observations, all-forcings or single-forcing experiments, or ice sheet models, to better understand the processes that drive SSS change. Given that the established salinity trend pattern is projected to intensify and that forced salinity change has major implications, including hydrologic cycle intensification, AMOC weakening, changes in ocean stratification, and greater-than-global regional sea level rise—such studies should be pursued with urgency.

Data availability statement

Sources of the model output are listed in table 1. Many of the fields analyzed here can also be found on a common grid in the MMLEAv2 for CESM1-LE, MPI-CMIP6-GE, CESM2-LE and GISS-E2-1-G (Maher 2025).

OISSSv2 data were obtained from https://doi.org/10.5067/SMP20-4UMCS.

IAP data were obtained from www.ocean.iap.ac.cn/pages/dataService/dataService.html. ERA5 data were obtained from https://cds.climate.copernicus.eu/datasets/reanalysis-era5-single-levels-monthly-means.

ERSSTv5 data were obtained from www.psl.noaa.gov/data/gridded/data.noaa.ersst.v5.html.

The data that supports the findings of this study are openly available in the public archives listed above.

Acknowledgment

The work described in this paper was primarily funded by the U.S. National Aeronautics and Space Administration (NASA) Oceanography Program, grant 80NSSC23K0358, which supported DPS, JEK, and YD. NM received support from the Australian Research Council Discovery Early Career Researcher Award (DE230100315). AC was supported by the National Oceanic and Atmospheric Administration (NOAA) Climate Program Office Climate Variability and Predictability program (CVP), award #NA24OARX431C0024-T1-01. This work made extensive use of the National Science Foundation National Center for Atmospheric Research (NSF NCAR) Community Earth System Model (CESM), and the authors thank the team of scientists, engineers, and administrators who develop the model, design experiments, and make the output publicly available. We also used output from additional models that is hosted within the Multimodel LE Archive, version 2 (MMLEAv2; Maher *et al* 2025), the creation of which was partially supported by the NASA grant and is distributed through the NSF NCAR Research Data Archive. To process, analyze, and visualize the data, we used a combination of netCDF operators, Climate Data Operators, python, and the NCAR Command Language (NCL; doi://10.5065/D6WD3XH5). We acknowledge computing support from the Casper system (doi:10.5065-qx9a-pg09) provided by the NSF NCAR.

ORCID iDs

David P Schneider 0000-0001-5308-1834
Nicola Maher 0000-0003-3922-9833
Yue Dong 0000-0001-6404-3446
Jennifer E Kay 0000-0002-3625-5377
Antonietta Capotondi 0000-0002-3594-5472

References

Armour K C *et al* 2024 Sea-surface temperature pattern effects have slowed global warming and biased warming-based constraints on climate sensitivity *Proc. Natl Acad. Sci. USA* **121** e2312093121

Baker J A, Bell M J, Jackson L C, Vallis G K, Watson A J and Wood R A 2025 Continued Atlantic overturning circulation even under climate extremes *Nature* **638** 987–94

Bao S, Wang H, Zhang R, Yan H and Chen J 2019 Comparison of satellite-derived sea surface salinity products from SMOS, aquarius, and SMAP *J. Geophys. Res.* **124** 1932–44

Capotondi A, Alexander M A, Bond N A, Curchitser E N and Scott J D 2012 Enhanced upper ocean stratification with climate change in the CMIP3 models *J. Geophys. Res.* **117** 1–23

Capotondi A, Deser C, Phillips A S, Okumura Y and Larson S M 2020 ENSO and Pacific decadal variability in the community earth system model version 2 *J. Adv. Model. Earth Syst.* **12** e2019MS002022

Cheng L, Trenberth K E, Gruber N, Abraham J P, Fasullo J T, Li G, Mann M E, Zhao X and Zhu J 2020 Improved estimates of changes in upper ocean salinity and the hydrological cycle *J. Clim.* **33** 10357–81

Craig P M, Ferreira D and Methven J 2023 A lagrangian perspective on the Atlantic and Pacific precipitation-evaporation asymmetry *J. Geophys. Res.* **128** e2023JD039087

Danabasoglu G *et al* 2020 The community earth system model version 2 (CESM2) *J. Adv. Model. Earth Syst.* **12** e2019MS001916

IBS Center for Climate Physics, National Center for Atmospheric Research, Danabasoglu G, Deser C, Rodgers K and Timmermann A 2021 CESM2 large ensemble community project (https://doi.org/10.26024/KGMP-C556)

DeRepentigny P, Jahn A, Holland M M and Smith A 2020 Arctic sea ice in two configurations of the CESM2 During the 20th and 21st centuries *J. Geophys. Res.* **125** e2020JC016133

Deser C *et al* 2020 Insights from Earth system model initial-condition large ensembles and future prospects *Nat. Clim. Change* **10** 277–86

Deser C, Phillips A S, Simpson I R, Rosenbloom N, Coleman D, Lehner F, Pendergrass A G, DiNezio P and Stevenson S 2020a Isolating the evolving contributions of anthropogenic aerosols and greenhouse gases: a new CESM1 large ensemble community resource *J. Clim.* **33** 7835–58

Dong Y, Kay J E, Deser C, Capotondi A and Sanchez S C 2024 Distilling the evolving contributions of anthropogenic aerosols and greenhouse gases to large-scale low-frequency surface ocean changes over the past century *Geophys. Res. Lett.* **51** e2024GL112020

Dong Y, Pauling A G, Sadai S and Armour K C 2022 Antarctic ice-sheet meltwater reduces transient warming and climate sensitivity through the sea-surface temperature pattern effect *Geophys. Res. Lett.* **49** e2022GL101249

Douville H and Cheng L 2024 Asymmetric sea surface salinity response to global warming: "fresh gets fresher but salty hesitates" *Geophys. Res. Lett.* **51** e2023GL107944

Durack P J, Wijffels S E and Matear R J 2012 Ocean salinities reveal strong global water cycle intensification during 1950–2000 *Science* **336** 455–8

Hawkins E and Sutton R 2012 Time of emergence of climate signals *Geophys. Res. Lett.* **39** 1–6

Hegerl G C, Brönnimann S, Cowan T, Friedman A R, Hawkins E, Iles C, Müller W, Schurer A and Undorf S 2019 Causes of climate change over the historical record *Environ. Res. Lett.* **14** 123006

Hersbach H *et al* 2020 The ERA5 global reanalysis *Quart. J. R. Meteorol. Soc.* **146** 1999–2049

Huang B, Thorne P W, Banzon V F, Boyer T, Chepurin G, Lawrimore J H, Menne M J, Smith T M, Vose R S and Zhang H-M 2017 Extended reconstructed sea surface temperature, version 5 (ERSSTv5): upgrades, validations, and intercomparisons *J. Clim.* **30** 8179–205

IPRC/SOEST University of Hawaii 2023 Multi-mission optimally interpolated sea surface salinity monthly global dataset V2 (https://doi.org/10.5067/SMP20-4UMCS)

Kay J E *et al* 2015 The Community Earth System Model (CESM) large ensemble project: a community resource for studying climate change in the presence of internal climate variability *Bull. Am. Meteorol. Soc.* **96** 1333–49

Kay J, Deser C, Phillips A and Simpson I 2025 CESM1 large ensemble community project (https://doi.org/10.5065/D6J101D1)

Kelley M *et al* 2020 GISS- 2.1: configurations and climatology *J. Adv. Model. Earth Syst.* **12** e2019MS002025

Lehner F, Deser C, Maher N, Marotzke J, Fischer E M, Brunner L, Knutti R and Hawkins E 2020 Partitioning climate projection uncertainty with multiple large ensembles and CMIP5/6 *Earth Syst. Dyn.* **11** 491–508

Li H and Fedorov A V 2021 Persistent freshening of the Arctic Ocean and changes in the North Atlantic salinity caused by Arctic sea ice decline *Clim. Dyn.* **57** 2995–3013

Li K-Y and Liu W 2025 Weakened Atlantic meridional overturning circulation causes the historical North Atlantic warming hole *Commun. Earth Environ.* **6** 416

Lu Y, Li Y, Lin P, Cheng L, Ge K, Liu H, Duan J and Wang F 2024 North Atlantic–Pacific salinity contrast enhanced by wind and ocean warming *Nat. Clim. Change* **14** 723–31

Maher N 2025 Multi-model large ensemble archive version 2 *Geoscience Data Exchange at the National Center for Atmospheric Research* (available at: https://gdex.ucar.edu/datasets/d651039/)

Maher N, Lehner F and Marotzke J 2020 Quantifying the role of internal variability in the temperature we expect to observe in the coming decades *Environ. Res. Lett.* **15** 054014

Maher N, Phillips A S, Deser C, Wills R C J, Lehner F, Fasullo J, Caron J M, Brunner L and Beyerle U 2025 The updated multi-model large ensemble archive and the climate variability diagnostics package: new tools for the study of climate variability and change *EGUsphere* accepted (https://doi.org/10.5194/egusphere-2024-3684)

Melnichenko O, Hacker P, Maximenko N, Lagerloef G and Potemra J 2016 Optimum interpolation analysis of Aquarius sea surface salinity *J. Geophys. Res.* **121** 602–16

Melnichenko O, Hacker P, Meissner T and Wentz F 2021 Aquarius/SMAP sea surface salinity optimum interpolation analysis IPRC Technical Note No. 7 (available at: https://apdrc.soest.hawaii.edu/doc/OISSS_Product_Notes.pdf)

Olonscheck D *et al* 2023 The new Max Planck Institute grand ensemble with CMIP6 forcing and high-frequency model output *J. Adv. Model. Earth Syst.* **15** e2023MS003790

Roach L A, Mankoff K D, Romanou A, Blanchard-Wrigglesworth E, Haine T W N and Schmidt Gavin A 2023 Winds and meltwater together lead to Southern Ocean surface cooling and sea ice expansion *Geophys. Res. Lett.* **50** e2023GL105948

Rodgers K B *et al* 2021 Ubiquity of human-induced changes in climate variability *Earth Syst. Dyn.* **12** 1393–411

Rye C D, Marshall J, Kelley M, Russell G, Nazarenko L S, Kostov Y, Schmidt G A and Hansen J 2020 Antarctic glacial melt as a driver of recent Southern Ocean climate trends *Geophys. Res. Lett.* **47** e2019GL086892

Sadai S, Condron A, DeConto R and Pollard D 2020 Future climate response to Antarctic ice sheet melt caused by anthropogenic warming *Sci. Adv.* **6** eaaz1169

Schlunegger S *et al* 2020 Time of emergence and large ensemble intercomparison for ocean biogeochemical trends *Glob. Biogeochem. Cycles* **34** e2019GB006453

Schmidt G A, Romanou A, Roach L A, Mankoff K D, Li Q, Rye C D, Kelley M, Marshall J C and Busecke J J M 2023 Anomalous meltwater from ice sheets and ice shelves is a historical forcing *Geophys. Res. Lett.* **50** e2023GL106530

Schmitt R 2008 Salinity and the global water cycle *Oceanography* **21** 12–19

Shiogama H, Tatebe H, Hayashi M, Abe M, Arai M, Koyama H, Imada Y, Kosaka Y, Ogura T and Watanabe M 2023 MIROC6 large ensemble (MIROC6-LE): experimental design and initial analyses *Earth Syst. Dyn.* **14** 1107–24

Silvy Y, Guilyardi E, Sallée J-B and Durack P J 2020 Human-induced changes to the global ocean water masses and their time of emergence *Nat. Clim. Change* **10** 1030–6

Simpson I R *et al* 2023 The CESM2 single-forcing large ensemble and comparison to CESM1: implications for experimental design *J. Clim.* **36** 5687–711

Simpson I and Rosenbloom N 2022 CESM2 single forcing large ensemble project (https://doi.org/10.26024/YW4W-1W27)

Singh H K A, Donohoe A, Bitz C M, Nusbaumer J and Noone D C 2016 Greater aerial moisture transport distances with warming amplify interbasin salinity contrasts *Geophys. Res. Lett.* **43** 8677–84

Skliris N, Zika J D, Nurser G, Josey S A and Marsh R 2016 Global water cycle amplifying at less than the Clausius-Clapeyron rate *Sci. Rep.* **6** 38752

Terray L, Corre L, Cravatte S, Delcroix T, Reverdin G and Ribes A 2012 Near-surface salinity as nature's rain gauge to detect human influence on the tropical water cycle *J. Clim.* **25** 958–77

Wei H, Subramanian A C, Karnauskas K B, DeMott C A, Mazloff M R and Balmaseda M A 2021 Tropical Pacific Air-sea interaction processes and biases in CESM2 and their relation to El Niño development *J. Geophys. Res.* **126** e2020JC016967

Wills R C J, Dong Y, Proistosecu C, Armour K C and Battisti D S 2022 Systematic climate model biases in the large-scale patterns of recent sea-surface temperature and sea-level pressure change *Geophys. Res. Lett.* **49** e2022GL100011

Wodzicki K R and Rapp A D 2016 Long-term characterization of the Pacific ITCZ using TRMM, GPCP, and ERA-Interim *J. Geophys. Res.* **121** 3153–70

Yeager S G, Chang P, Danabasoglu G, Rosenbloom N, Zhang Q, Castruccio F S, Gopal A, Cameron Rencurrel M and Simpson I R 2023 Reduced Southern Ocean warming enhances global skill and signal-to-noise in an eddy-resolving decadal prediction system *npj Clim. Atmos Sci.* **6** 107

Zhu C and Liu Z 2020 Weakening Atlantic overturning circulation causes South Atlantic salinity pile-up *Nat. Clim. Change* **10** 998–1003

Zhu C, Liu Z, Zhang S and Wu L 2023 Likely accelerated weakening of Atlantic overturning circulation emerges in optimal salinity fingerprint *Nat. Commun.* **14** 1245